metals

MDPI

Article

Impact of Submerged Entry Nozzle (SEN) Immersion Depth on Meniscus Flow in Continuous Casting Mold under Electromagnetic Brake (EMBr)

Alexander Vakhrushev [1], Ebrahim Karimi-Sibaki [1], Jan Bohacek [2], Menghuai Wu [3], Andreas Ludwig [3], Yong Tang [4], Gernot Hackl [4], Gerald Nitzl [5], Josef Watzinger [6] and Abdellah Kharicha [1,*]

1 Christian-Doppler Laboratory for Metallurgical Applications of Magnetohydrodynamics, Montanuniversität Leoben, 8700 Leoben, Austria
2 Heat Transfer and Fluid Flow Laboratory, Faculty of Mechanical Engineering, Brno University of Technology, 61669 Brno, Czech Republic
3 Chair of Simulation and Modeling of Metallurgical Processes, Department of Metallurgy, Montanuniversität Leoben, 8700 Leoben, Austria
4 RHI Magnesita GmbH, 8700 Leoben, Austria
5 RHI Magnesita GmbH, 1120 Vienna, Austria
6 Primetals Technologies, 4031 Linz, Austria
* Correspondence: abdellah.kharicha@unileoben.ac.at

Abstract: Complex multi-phase phenomena, including turbulent flow, solidification, and magnetohydrodynamics (MHD) forces, occur during the continuous casting (CC) under the applied electromagnetic brake (EMBr). The results of the small-scale experiment of the liquid metal model for continuous casting (mini-LIMMCAST) at the Helmholtz-Zentrum Dresden-Rossendorf (HZDR), investigating MHD flow with a deep immersion depth of 100 mm, are supplemented by newly presented numerical studies with the shallow position of the submerged entry nozzle (SEN) at 50 mm below the meniscus. Herein, the focus is on the MHD effects at the meniscus level considering (i) a fully insulating domain boundary, (ii) a perfectly conductive mold, or (iii) the presence of the solid shell. The volume-of-fluid (VOF) approach is utilized to model a Galinstan flow, including free surface behavior. A multiphase solver is developed using conservative MHD formulations in the framework of the open-source computational fluid dynamics (CFD) package OpenFOAM®. The wall-adapting local eddy-viscosity (WALE) subgrid-scale (SGS) model is employed to model the turbulent effects on the free surface flow. We found that, for the deep immersion depth, the meniscus remains calm under the EMBr for the conductive and semi-conductive domain. For the insulated mold disregarding the SEN position, the self-inducing MHD vortices, aligned with the magnetic field, cause strong waving of the meniscus and air bubble entrapment for shallow immersion depth. Secondary MHD structures can form close to the meniscus under specific conditions. The influence of the EMBr and immersion depth on the flow energy characteristics is analyzed using power spectral density (PSD).

Keywords: magnetohydrodynamics (MHD); turbulence; meniscus flow; volume-of-fluid (VOF); electromagnetic brake (EMBr); continuous casting mold; OpenFOAM®

check for updates

Citation: Vakhrushev, A.; Karimi-Sibaki, E.; Bohacek, J.; Wu, M.; Ludwig, A.; Tang, Y.; Hackl, G.; Nitzl, G.; Watzinger, J.; Kharicha, A. Impact of Submerged Entry Nozzle (SEN) Immersion Depth on Meniscus Flow in Continuous Casting Mold under Electromagnetic Brake (EMBr). *Metals* **2023**, *13*, 444. https://doi.org/10.3390/met13030444

Academic Editors: Ricardo J. Alves de Sousa and Mehdi Safari

Received: 25 January 2023
Revised: 9 February 2023
Accepted: 15 February 2023
Published: 21 February 2023

Copyright: © 2023 by the authors. Licensee MDPI, Basel, Switzerland. This article is an open access article distributed under the terms and conditions of the Creative Commons Attribution (CC BY) license (https://creativecommons.org/licenses/by/4.0/).

1. Introduction

The continuous casting (CC) process involves complex multi-phase phenomena such as turbulent flow, free surface waving, solidification, magnetohydrodynamics (MHD) forces exerted by electromagnetic braking (EMBr), etc. [1–4]. These combined phenomena can exhibit unpredictable behavior, resulting in the formation of defects or breakouts.

The steel producers aim at increasing production rates while maintaining the essential quality level of the final product. However, the increase in casting speeds can lead to an enhanced risk of slag entrainment, which is one of the main sources of inclusion defects in

the CC process. Hibbeler and Thomas [5] identified distinct mechanisms of the mold flux entrainment, such as level fluctuations, meniscus freezing, vortexing, shear instabilities, argon gas injections, etc. A common issue of the slag open eye formation due to the gas injection were carefully studied by Liu et al. [6] as well by Srivastava et al. [7]. Different mold flow phenomena, leading to the slag engulfment, were investigated in pioneering experiments of Iguchi and co-authors [8–11], and more recently by Hagemann et al. [12], by Puttinger, Saeedipour et al. [13,14]. The casting speed limitations based on the mechanical properties of the solid shell, the importance of the mold level and waving control, and the significance of the slag feeding uniformity were presented by Bernhard et al. [15].

The effective flow control technique, used for decades in the continuous casting industry, is the electromagnetic braking. It influences not only the flow structure but can also cause dendrite bending in the solidifying shell, as investigated by Sengupta et al. [16]. Nowadays, the EMBr frequently comes in combination with the electromagnetic stirring (EMS) [17]. It can be applied to stabilize and improve the asymmetric pattern occurring in the mold flow under different circumstances [18,19].

The presented investigation is based on the well-known mini-LIMMCAST experiment at the Helmholtz-Zentrum Dresden-Rossendorf (HZDR, Germany) employing the GaInSn alloy, which is liquid at room temperature [20,21]. It was often used in the numerical studies based on the single-phase approach [22–26].

The free surface behavior was previously modeled by Asad et al. [27] for the LIMMCAST experiment setup using the volume-of-fluid (VOF) approach implemented in the open-source CFD software OpenFOAM® [28], and a good overall agreement was found with the experimental measurements. Advanced filtering in the large eddy simulation (LES) of multiphase flows was recently applied using an approximate deconvolution model by Saeedipour, Vincent, and Pirker [29], improving the prediction of macroscopic flow characteristics compared with conventional models.

It should be mentioned that the best VOF results are achieved on the structured computational meshes. However, being constantly developed and improved, the geometric reconstruction techniques, such as the isoAdvector method presented by Rønby et al. [30] and validated for different applications [31,32], are the future for the effective modelling of the multiphase phenomena during the CC process on unstructured grids.

The comparative study of the MHD flow modelling using different commercial CFD packages and OpenFOAM® was presented in very details by Smolyanov et al. [33]. Particularly, they showed the drawbacks of applying the standard OpenFOAM® solver to the MHD flows. Based on the finite volume method (FVM), it calculates the MHD quantities in a non-conservative, cell-centered form. Therefore, a conservative Gauss-Green-type reconstruction of the induced electric current density and Lorentz force was used in the present study instead of the conventional cell-centered formulation. The parallelization capabilities, embedded in the vector-tensor framework of OpenFOAM®, were effectively used for the calculations on the high-resolution numerical grids.

As previously shown by the authors, the induced electric current density distribution [24,25] and the complex topology of the Lorentz force [26] are not limited to the damping of the jet flow, as is traditionally expected. Due to the closure of the e-current lines through the liquid bulk, the quiescent melt is brought into motion and is entrapped in the mean flow, causing the flattening of the jets and the formation of the accompanying reverse flow zones [34]. Thereby, the application of the magnetic field can cause the undesired instability of the free surface. Different scenarios of the multiphase turbulent MHD flow, including two SEN immersion depths of 100 mm and 50 mm, along with the assumptions of the (i) nonconductive, (ii) perfectly conductive, and (iii) semi-conductive domain boundaries, are modeled and analyzed in this work.

The presented study is focused on the EMBr effects at the meniscus level, comparing the results based on the immersion depth of the submerged entry nozzle (SEN) and considering the influence of the electrical conductivity of the growing solid shell. As it was shown, the hydrodynamical solution is tightly connected with the MHD boundary

conditions. A single mesh approach is applied for the first time for the MHD flows, combining the conductive solid with the VOF interface tracking. The presented multiphase model and analysis of the numerical results are the prerequisites for the simulation of the real CC process by coupling turbulent flow, solidification, MHD effects, and liquid slag behavior.

2. Materials and Methods

The governing equations of the applied multiphase numerical model of the unsteady incompressible turbulent flow using the mixture formulations are as follows,

$$\frac{\partial \rho}{\partial t} + \nabla \bullet \rho \boldsymbol{u} = 0, \tag{1}$$

$$\frac{\partial \rho \boldsymbol{u}}{\partial t} + \nabla \bullet (\rho \boldsymbol{u} \otimes \boldsymbol{u}) = -\nabla p + \rho \boldsymbol{g} + \nabla \bullet \boldsymbol{\tau}_{\text{lam}} - \nabla \bullet \boldsymbol{\tau}_{\text{SGS}} + \boldsymbol{S}_{\text{surf}} + \boldsymbol{F}_{\text{L}}, \tag{2}$$

where $\boldsymbol{u}$ is velocity; ρ is density; p is a pressure field; $\boldsymbol{g}$ is the gravitational constant; $\boldsymbol{\tau}_{\text{lam}}$ and $\boldsymbol{\tau}_{\text{SGS}}$ are the laminar and the subgrid-scale (SGS) Reynolds stress tensors, respectively. The SGS stress tensor is traditionally expressed through the modeled eddy-viscosity (ν_{SGS}) in a form of $\boldsymbol{\tau}_{\text{SGS}} = -\nu_{\text{SGS}} \cdot \left(\nabla \boldsymbol{u} + \nabla^{\text{T}} \boldsymbol{u}\right)$, which defines the negative sign in the diffusive term $\nabla \bullet \boldsymbol{\tau}_{\text{SGS}}$. The momentum Equation (2) includes the surface tension $\boldsymbol{S}_{\text{surf}}$ and the Lorentz force $\boldsymbol{F}_{\text{L}}$ acting in the conducting melt under the applied constant magnetic field $\boldsymbol{B}_0$. The buoyancy force is accounted by the Boussinesq approximation.

Since the magnetic Reynolds number is low for the CC applications ($\mathcal{R}m \ll 1$) [25], the Maxwell's equations are reduced using the electric potential method [35]

$$\boldsymbol{j} = \sigma \cdot (-\nabla \varphi + \boldsymbol{u} \times \boldsymbol{B}_0), \tag{3}$$

$$\nabla \bullet (\sigma \, \nabla \varphi) = \nabla \bullet (\sigma \cdot (\boldsymbol{u} \times \boldsymbol{B}_0)), \tag{4}$$

$$\boldsymbol{F}_{\text{L}} = \boldsymbol{j} \times \boldsymbol{B}_0, \tag{5}$$

where $\boldsymbol{j}$ is the induced electric current density, φ is the electric potential, and σ is electrical conductivity. A system of Equations (1)–(5) was solved based on the FVM framework of the open-source CFD package OpenFOAM®(OpenFOAM® version 8, OpenFOAM Foundation Ltd Incorporated, London, United Kingdom) [28] using an advanced face flux reconstruction scheme for the MHD Equations (3)–(5) described elsewhere [36].

The phase interface was tracked with the volume-of-fluid (VOF) approach introduced by Hirt and Nichols [37]. A standard two-phase OpenFOAM® solver, based on the PhD thesis of Ubbink [38] and his later publication with Issa [39], was used with the earlier modifications by the authors [40] and with a newly introduced MHD model that included the presence of a semi-conductive solid.

A two-phase melt/air mixture is defined by the corresponding volume fractions α_{i}:

$$\alpha_{\text{melt}} + \alpha_{\text{air}} = 1. \tag{6}$$

The mixture density and dynamic viscosity are calculated as a weighted average:

$$\rho = \alpha_{\text{melt}} \cdot \rho_{\text{melt}} + \alpha_{\text{air}} \cdot \rho_{\text{air}}, \tag{7}$$

$$\mu = \alpha_{\text{melt}} \cdot \mu_{\text{melt}} + \alpha_{\text{air}} \cdot \mu_{\text{air}}. \tag{8}$$

In the next formulations a single α-notation is used to represent the melt phase.

The continuum surface force (CSF) is given according to Brackbill et al. [41] by including the surface tension on the right-hand side of the momentum Equation (2):

$$\boldsymbol{S}_{\text{surf}} = \gamma \cdot \kappa \cdot \boldsymbol{n}, \tag{9}$$

where γ is the surface tension and $\boldsymbol{n}$ is the interface normal vector, calculated as

$$\boldsymbol{n} = \nabla\alpha. \tag{10}$$

The VOF gradient $\nabla\alpha \neq \mathbf{0}$ is continuous at the phase transitional area, whereas the interface curvature (κ) is expressed through integration of the unit normal vector:

$$\kappa = -\nabla\bullet\left(\frac{\nabla\alpha}{|\nabla\alpha|}\right). \tag{11}$$

The α-field propagates with the fluid as a Lagrangian invariant; thus, its material derivative is zero [37]:

$$\frac{D\alpha}{Dt} = \frac{\partial\alpha}{\partial t} + \boldsymbol{u}\bullet\nabla\alpha = 0. \tag{12}$$

The continuity Equation (1) is rearranged to the non-conservative form (see Equation (2.12) in Ubbink [38]) and, by substituting Equation (12), it is reduced to

$$\nabla\bullet\boldsymbol{u} = 0. \tag{13}$$

In its turn, a conservative form of the interface advection Equation (12) is applied:

$$\frac{\partial\alpha}{\partial t} + \nabla\bullet(\alpha\boldsymbol{u}) = 0. \tag{14}$$

The numerical approach for solving Equation (14) in the OpenFOAM® package is based on the flux-corrected transport technique from Boris and Book [42], with improvements by Zalesak [43]. It employs the multidimensional universal limiter with explicit solution (MULES) to keep the bounded solution of Equation (14).

For the proper treatment of the induced current density paths in the vicinity of the conducting/insulating phase interface, a special interpolation technique was used to calculate the electrical conductivity (σ) based on the liquid fraction (α). Details are described in the next section.

The applied numerical technique for the first time combines a previously developed single mesh approach, which includes the liquid melt bulk and the conductive solid on the same calculation grid [25], with the VOF method to track the phase interface.

The schematics of the modelling domain are outlined in Figure 1a. More details regarding the geometry and the dimensions of the mold and SEN can be found in refs. [22,23]. The geometry of the outflow channels in Figure 1a does not correspond one-to-one to the recirculation system in the mini-LIMMCAST experiment. The Galinstan is then pumped from a container to a tundish, and a stopper rod is used to control the flow rate through the SEN. The melt height in the tundish is maintained by adjusting the pump. The experimental loop is closed by a dam between the mold and the reservoir to maintain the meniscus level. Nevertheless, the shape and size of the outflow system in the simulation do not affect the melt flow inside the mold region.

The distribution of the EMBr field $\boldsymbol{B}_0$ is presented in Figure 1b. The maximum value of 312 mT is aligned with the bottom of the SEN well and corresponds to the EMBr case of 92 mm below the meniscus in Thomas et al. [23]. The immersion depth in this study is measured from the SEN bottom. Two immersion depths of 100 mm and 50 mm were combined with three different cases of the mold's electrical conductivity, as shown in Figure 1c. The deeper 100 mm Case A corresponds to the mini-LIMMCAST experiment [20,21] and was used in the numerical studies [22–26]. However, such an immersion depth, rescaled from the 1-to-6 GaInSn model, is significantly overestimated for the real continuous casting process. Thereby, the shallower 50 mm Case B is included to reflect more realistic scenarios. The meniscus level in Case A is defined by the outflows position. For Case B, a total pressure was applied to compensate a 50 mm column of Galinstan by exploiting the advantages of a virtual experiment when using the CFD technique.

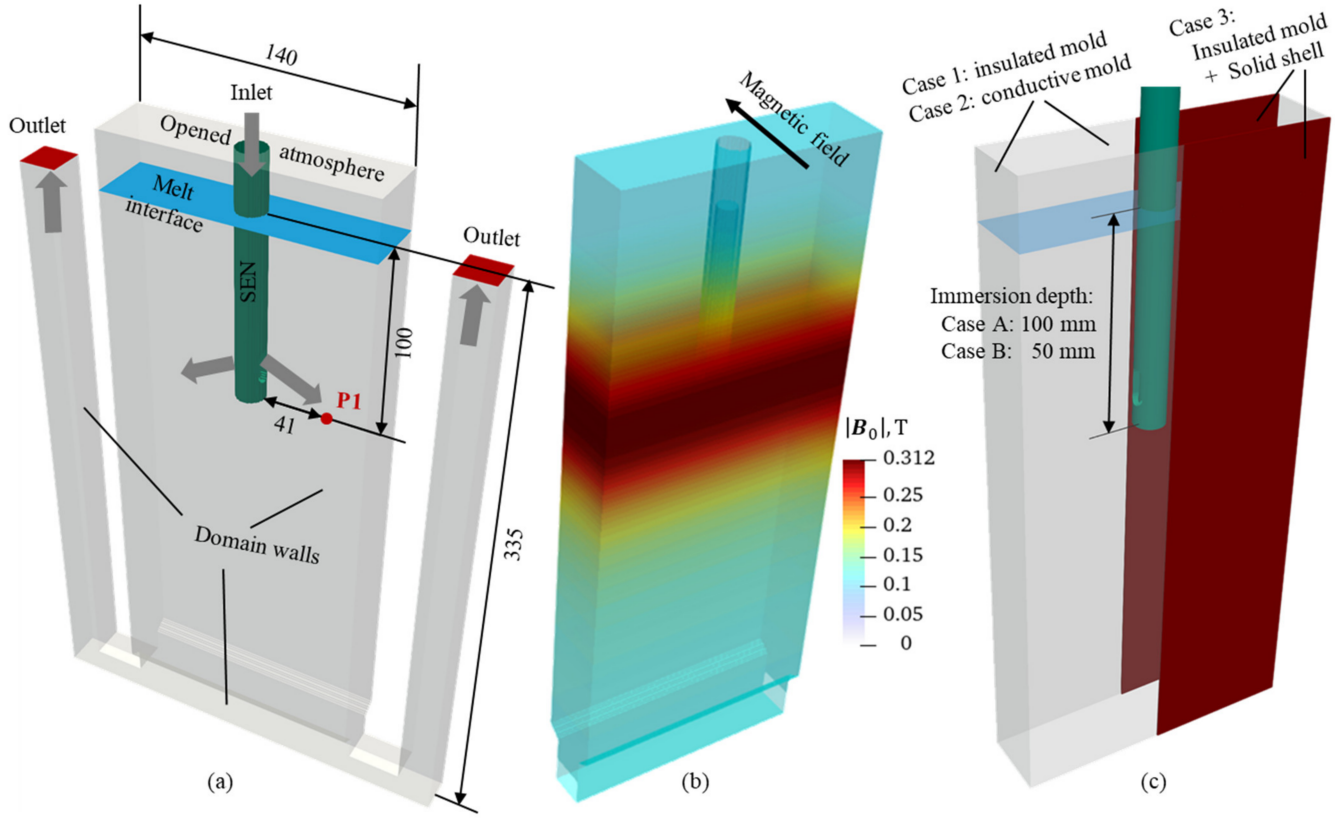


Figure 1. Modelling domain and settings: (**a**) geometry outline based on the mini-LIMMCAST experiment (data from [20,21]); (**b**) applied magnetic field; (**c**) simulated cases schematics.

The simulated cases are listed in Table 1. Two simulations without EMBr (Case 0A and Case 0B) are used for the comparison. The setups with the insulated mold (Case 1), with the ideally conductive boundaries (Case 2), and combining the insulated domain with the highly conductive solid (Case 3) were used for EMBr modelling. Index A corresponds to the 100 mm immersion depth, index B to the 50 mm depth. Cases 3A and 3B model a double skin effect in the real casting process, where the slag skin insulates the copper mold and the solid shell conducts the induced electric current. This phenomenon is detailed in the recent publications of the authors [24–26] based on the mini-LIMMCAST experiment, and with an application to the slab casting (TSC) [18,44,45]. The detailed process parameters and material properties are presented elsewhere [20,21,23,46].

Table 1. Outline of the simulated cases.

Case Name	Immersion Depth (mm)	EMBr Power (mT)	Domain Electrical Conductivity
Case 0A	100	0	-
Case 0B	50	0	-
Case 1A	100	312	Insulated mold
Case 2A	100	312	Conductive mold
Case 3A	100	312	Insulated mold with shell
Case 1B	50	312	Insulated mold
Case 2B	50	312	Conductive mold
Case 3B	50	312	Insulated mold with shell

Two theoretical cases with the perfectly insulated or conductive mold show the extreme MHD flow effects as a reference. They are compared with a scenario with a finite solid shell conductance ratio of 0.13 (Cases 3A and 3B), which is typical for CC. The top region of the real mold comprises most of the EMBr action. The solidifying shell is still thin, as

presented in Figure 16 from Vakhrushev et al. [25]. It is crucial to clarify that the solid shell in the mold region has a limited capacity to conduct the induced e-current and to enhance the braking effect from the applied magnetic field. The alloy composition, shell thickness, and corresponding conductance ratio are the inputs, not the control parameters, to model the EMBr effects in the CC process. This understanding can be stripped from the readers if the conductance ratio is continuously varied in a numerical study. Considering the EMBr power, magnetic field distribution, and its variation as a valid control parameters provides clear guidelines for the CC process optimization.

3. Results

3.1. Handling Electrical Conductivity on Interface

In the presented study, the interface between the strongly conducting liquid (GaInSn melt) and the insulating gas phase (air) is simulated. Since the VOF approach uses averaged media properties, a proper interpolation of the electrical conductivity σ is required as a function of the liquid fraction α.

Figure 2a shows different interpolation results of the dimensionless conductivity $\overline{\sigma}(\alpha)$, which is normalized between 0 and 1 regardless of the ratio between the melt conductivity (σ_{melt}) and the air phase conductivity (σ_{air}):

$$\overline{\sigma}(\alpha) = \frac{\sigma(\alpha) - \sigma_{\text{air}}}{\sigma_{\text{melt}} - \sigma_{\text{air}}}. \tag{15}$$

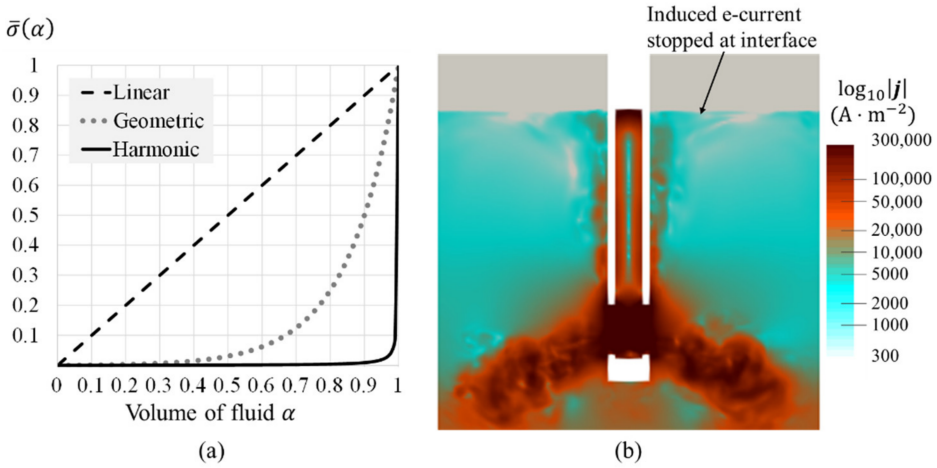


Figure 2. Electrical conductivity at the interface: (**a**) comparison of the linear, geometric, and harmonic interpolations; (**b**) induced e-current density (harmonic interpolation of the e-conductivity).

As can be seen from Figure 2a, the standard linear interpolation results in the overestimated σ. The Galinstan conductivity $\sigma_{\text{melt}} = 3.2 \times 10^6\ \Omega^{-1}\text{m}^{-1}$ [23], which is at least 15 orders of magnitude greater than $\sigma_{\text{air}} = 10^{-15} \ldots 10^{-9}\Omega^{-1}\text{m}^{-1}$ [47], prevails in linear weighting starting from the low liquid fraction.

The preliminary simulations, employing linear interpolation, approved that the induced e-current was able to cross the interface. The conductivity of the entrapped air bubbles did not vary significantly regarding the melt properties, and the e-current lines were not affected. Thus, two additional interpolation schemes were examined:

$$\text{geometric weighted mean } \sigma(\alpha) = (\sigma_{\text{melt}})^{\alpha}(\sigma_{\text{air}})^{1-\alpha}, \tag{16}$$

$$\text{harmonic weighted mean } \sigma(\alpha) = 1/[\alpha/\sigma_{\text{melt}} + (1-\alpha)/\sigma_{\text{air}}]. \tag{17}$$

The geometric averaging gives more difference between two phases at the α interval between 0 and 0.4, whereas the harmonic mean is very close to the step function, as shown in Figure 2a. Numerical studies using both schemes showed that the geometric

interpolation is very robust, providing stability to the solution procedure. On the other hand, the harmonic averaging led to instability issues, which were solved using under-relaxation of the electric conductivity σ and electric potential φ fields. As a result, the induced electric current density was only restricted to the melt region and was stopped at the melt/air interface, as shown in Figure 2b. The harmonic interpolation of the electrical conductivity was used hereinafter for the presented studies.

3.2. Model Verification

The cases with a SEN immersion depth of 100 mm were compared against the experimental measurements [20–23]. Simulations without a magnetic field (Case 0A) and with the applied EMBr (Case 3A) are shown in Figures 3 and 4, correspondingly, with the probe lines marked at 90, 100, and 110 mm below the meniscus.

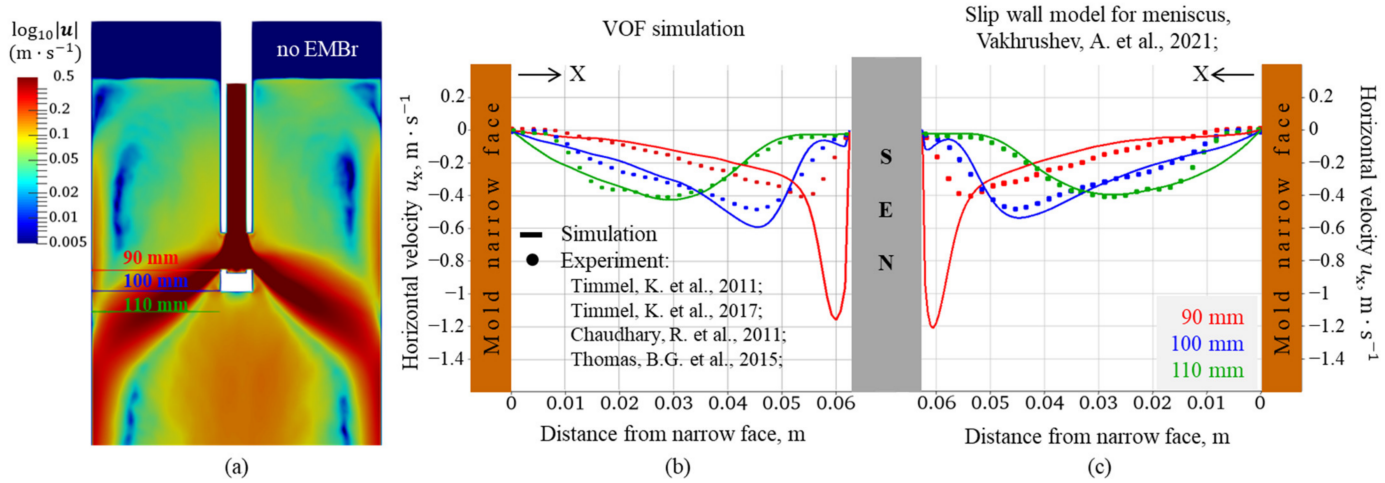


Figure 3. Verification of the simulation results without EMBr (Case 0A): (**a**) time-averaged melt velocity (midplane); horizontal velocity (**b**) in this study (experimental data from [20–23]) and (**c**) in the previous publication data from [26].

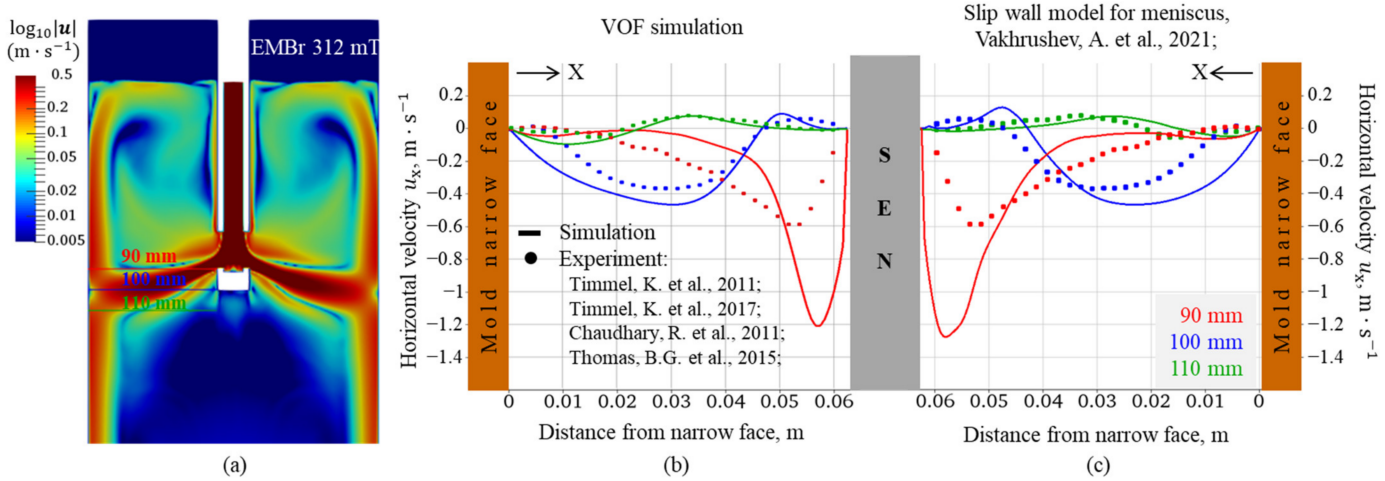


Figure 4. Verification of the simulation results with EMBr (Case 3A): (**a**) time-averaged melt velocity (midplane); horizontal velocity (**b**) in this study (experimental data from [20–23]) and (**c**) in the previous publication data from [26].

Model verification showed a very good agreement with the single-phase simulations [26], which additionally indicates that such a deep SEN immersion depth diminishes the free surface effect in the mold flow, which is not detected in the industrial CC practice. The deviation from the experiment is at the same level as in other research [22,23].

3.3. Case Studies

The velocity fields without applied EMBr for the immersion depths of 100 mm (Case 0A) and 50 mm (Case 0B) are illustrated in Figure 5a,b. The flow accelerates and becomes more turbulent near the meniscus when the jets dispatch closer to the top surface (Figure 5b,d).

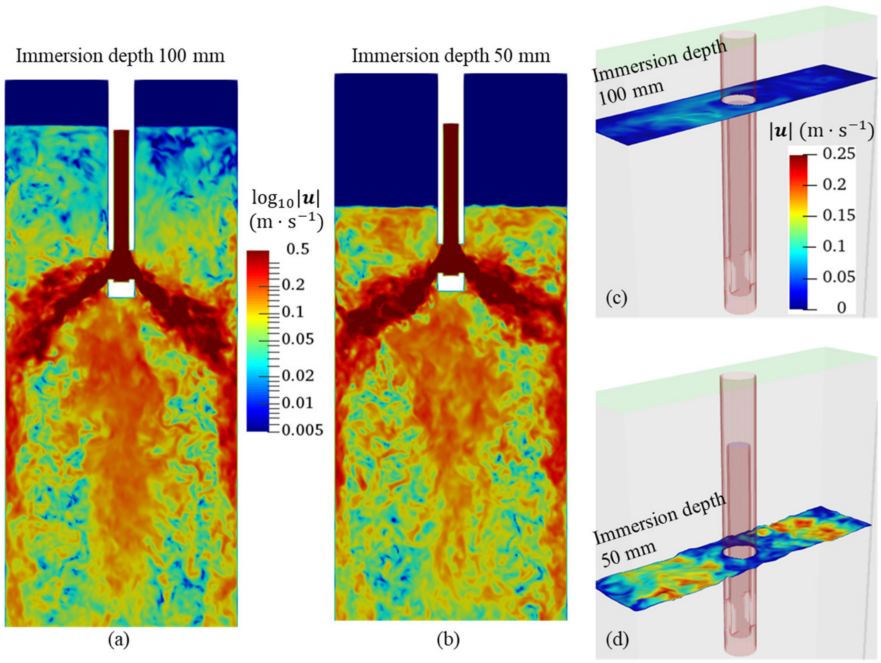


Figure 5. Modelling results for the non-EMBr Case 0A and Case 0B: (**a**,**b**) melt velocity (midplane); (**c**,**d**) velocity magnitude at the melt/air interface.

Before discussing the MHD modelling results, it is mandatory to remind the readers of the induced electric current distribution taking into account the domain boundary conductivity, recently detailed in the study [25] and recalled here in Figure 6.

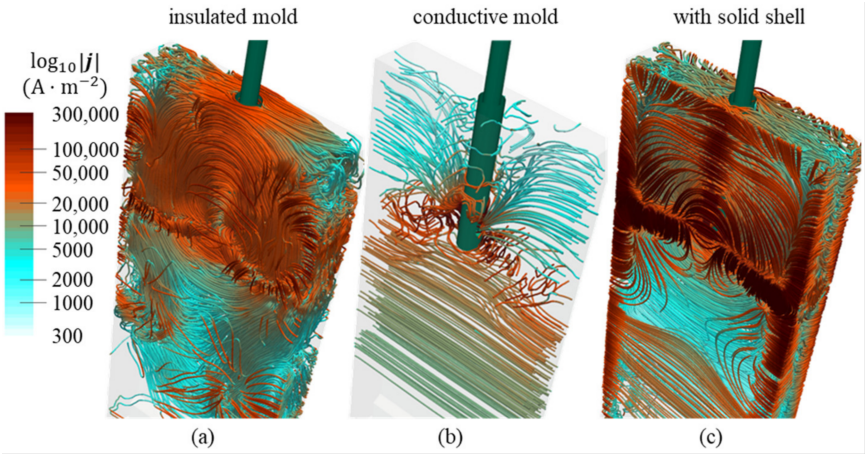


Figure 6. Induced e-current lines distribution: (**a**) fully insulated mold; (**b**) perfectly conductive mold; (**c**) presence of the conductive solid shell. Extracted from Ref. [25]. Reference [25] is available under Creative Commons By Attribution 4.0 in: https://creativecommons.org/licenses/by/4.0/, accessed on 19 February 2023.

In the case of the fully insulated domain (Case 1A), the induced current lines are forced to close through the liquid bulk, as shown in Figure 6a. The surrounding liquid is brought into motion [34,35], and self-inducing vortex structures are initiated, destabilizing the flow.

When the mold is perfectly conductive (Case 2A), the e-current goes directly into the walls (Figure 6b), leading to an excessive braking force compared with the porous resistance. In the presence of a semi-conductive shell (Case 3A), the e-current tends to close through the solid (Figure 6c), which results in moderate braking effects.

In the following, modelling results for the cases under EMBr with different SEN immersion depths are presented. Starting with the insulated mold scenario (Case 1A) with the 100 mm SEN immersion depth, the induced e-current density (Figure 7a) and velocity (Figure 7b) distributions are shown in the midplane. The meniscus velocity under the EMBr (Figure 7c) is compared with the case without an applied magnetic field (Figure 7d). To effectively demonstrate the velocity field at the interface, the free surface velocities are linearly scaled between 0 and 0.25 m/s.

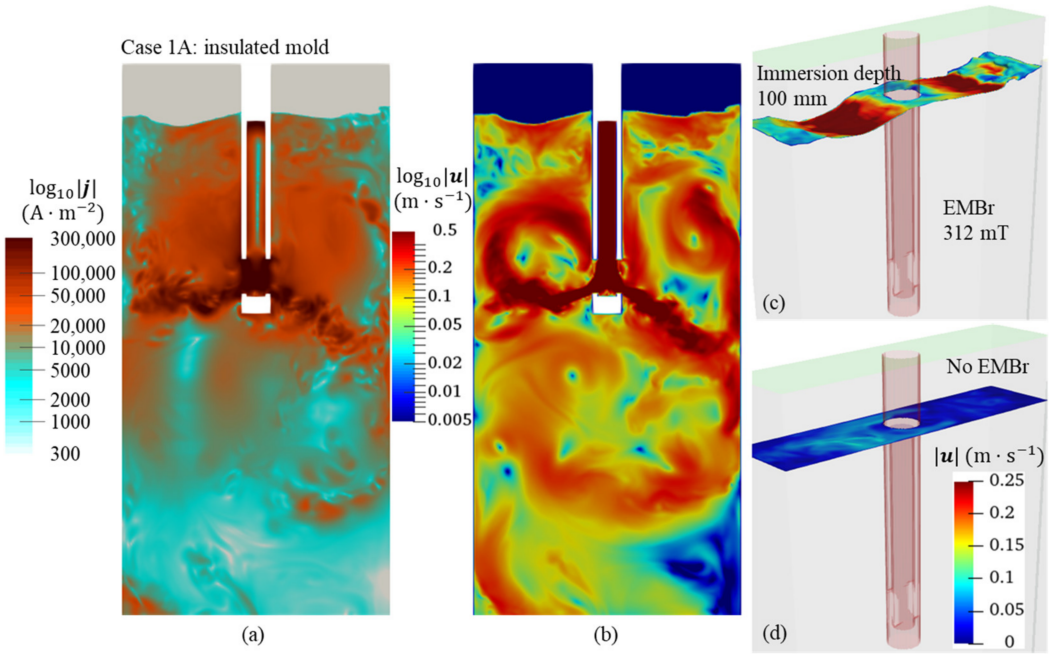


Figure 7. Meniscus flow for Case 1A: (**a**) induced e-current density and (**b**) melt velocity (midplane); (**c**) interface velocity with EMBr compared with (**d**) Case 0A without EMBr.

The strong induced e-current, generated by the feeding jets, closes through the liquid bulk, concentrating in the upper region of the mold, as shown in Figure 7a. The self-inducing vortex structures travel across the mold, causing jets to oscillate and destabilizing the meniscus (Figure 7a). Free surface velocities, shown in Figure 7c, are accelerated in comparison to a calmer non-EMBr case in Figure 7d; a strong wave is detected.

When the DC magnetic field is imposed on a perfectly conductive domain (Case 2A in Figure 8), the induced e-current flows directly towards the conductive walls. The upper part of the melt bulk is almost current-free apart from the cylindric sublayer adjoint to the insulated SEN shroud. Most of the e-current density is concentrated around the jets and in the lower region. The corresponding field distribution is displayed in Figure 8a.

Due to the "attachment" of the e-current to the conductive walls, a strong braking force occurs, as discussed in the previous section. That results in a flow stagnation zone in the upper region of the CC mold and leads to the formation of the plug-type velocity distribution below the SEN location (see Figure 8b). The meniscus becomes calmer (Figure 8c) under the applied magnetic field and with the deep SEN immersion depth, despite the upward flow initiated along the insulating SEN wall, which is detailed later.

A complex phenomenon is described when a conductive solid shell is attached to the insulting CC mold (see Case 3A in Figure 9). The induced e-current loops tend to go through the highly conductive solid, as previously illustrated in Figure 6c. That leads to a moderate braking of the flow compared with Case 2A. The induced e-current (Figure 9a) partially

closes through the liquid bulk, similar to Case 1A, although its net value significantly drops. However, that is sufficient for the decent melt mixing, which is desirable in the industrial process, since it promotes the super heat transport towards meniscus, decreases macrosegregation, etc.

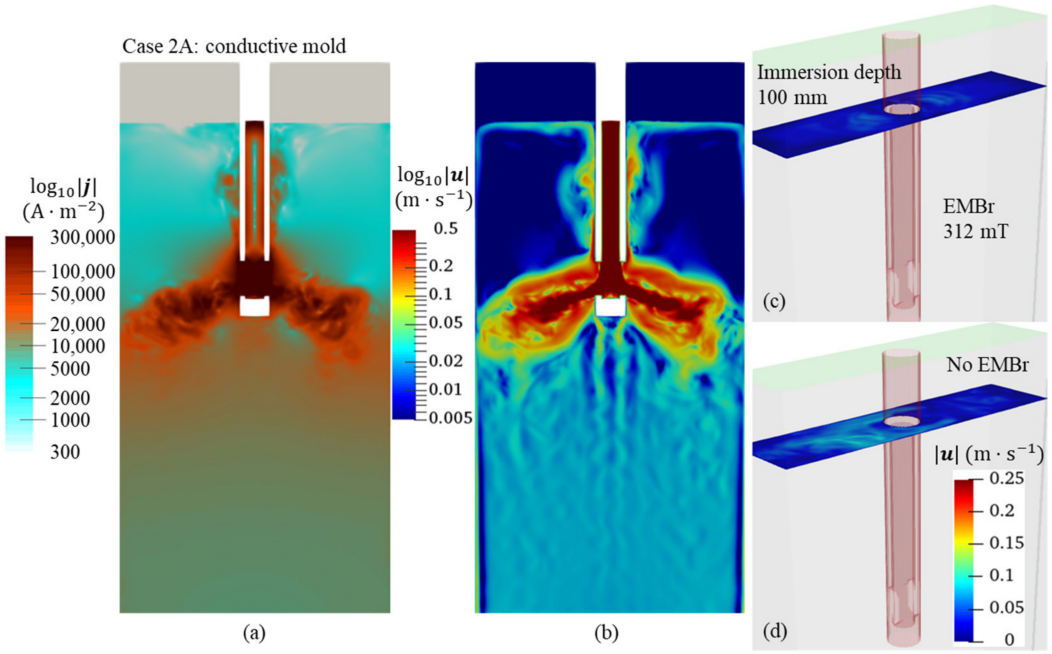


Figure 8. Meniscus flow for Case 2A: (**a**) induced e-current density and (**b**) melt velocity (midplane); (**c**) interface velocity with EMBr compared with (**d**) Case 0A without EMBr.

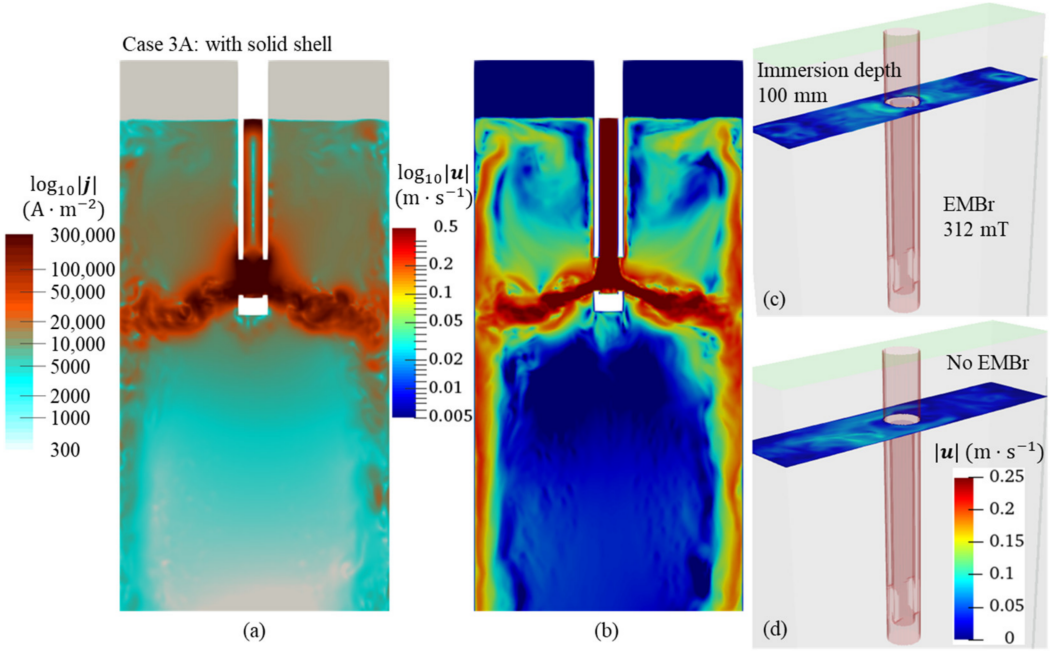


Figure 9. Meniscus flow for Case 3A: (**a**) induced e-current density and (**b**) melt velocity (midplane); (**c**) interface velocity with EMBr compared with (**d**) Case 0A without EMBr.

The top surface remains calm under the EMBr (Figure 9c), with the same submeniscus velocities and intensities as in the case without the magnetic field (Figure 9d). However, the flow pattern totally differs from the double roll due to the formation of the opposite vortex along the SEN [26]. No slowdown of the subsurface velocity occurs as it was observed in

Case 2A with the conductive mold (Figure 8). That happens due to the restructuring of the turbulence into a quasi-2D state, as detailed in the next section.

To sum up, in the case of the deep SEN immersion depth, the jet flow noticeably affects top surface behavior only in the insulated domain and under EMBr.

In the following, the MHD flow results for the shallower SEN position at 50 mm below the meniscus are presented.

When the magnetic field is applied to the electrically insulated domain (Case 1B, Figure 10), strong flow instabilities are developed, similar to the case with the immersion depth of 100 mm. However, with the shallow SEN position, the generated MHD vortices directly interact with the free surface. Meniscus distortions become critical and lead to air bubble entrapment, as shown in Figure 10c. Conversely, the characteristic size of the coherent structures decreases in comparison to Case 1A since they are restricted by the free surface. That is also reflected by the change in the spectral density distribution, described in the next section.

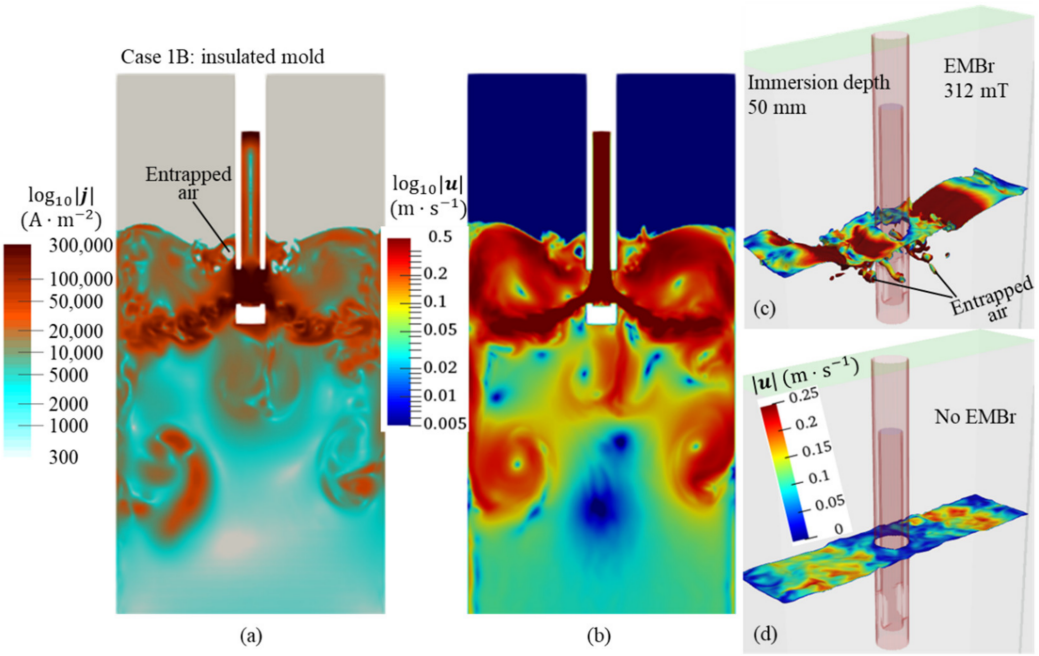


Figure 10. Meniscus flow for Case 1B: (**a**) induced e-current density and (**b**) melt velocity (midplane); (**c**) interface velocity with EMBr compared with (**d**) Case 0B without EMBr.

The benefit of using the advanced VOF interpolation of the electrical conductivity, as suggested in this study, is clearly displayed by the induced e-current density field in Figure 10a. The entrapped air bubbles are properly treated as an insulating medium by the numerical model. The induced currents are not diffused at the phase boundary, and they are prohibited from closing through the gas phase.

A free surface is strongly affected by the upward flow along the insulated SEN outer surface induced by EMBr in the shallower Case 2B in Figure 11 in comparison to the 100 mm Case 2A. Since the distance to the top surface is shorter, that causes a hefty interaction with the meniscus and acceleration of the submeniscus flow. As a result, the top surface wave is slightly higher than in the non-EMBr scenario in Figure 11d. The melt velocities remain at the same level in Figure 11c,d. Consequently, the meniscus flow direction in Case 2B is opposing the traditional double-roll pattern.

The modelling results for the Case 3B with the attached solid shell are shown in Figure 12. In comparison to the similar scenario with the SEN immersion depth of 100 mm in Figure 9, the strong interaction of the upper rolls with the meniscus is detected. The upper rolls under the EMBr in Figure 12c are aligned with the magnetic field direction, and a corresponding wave shape is observed.

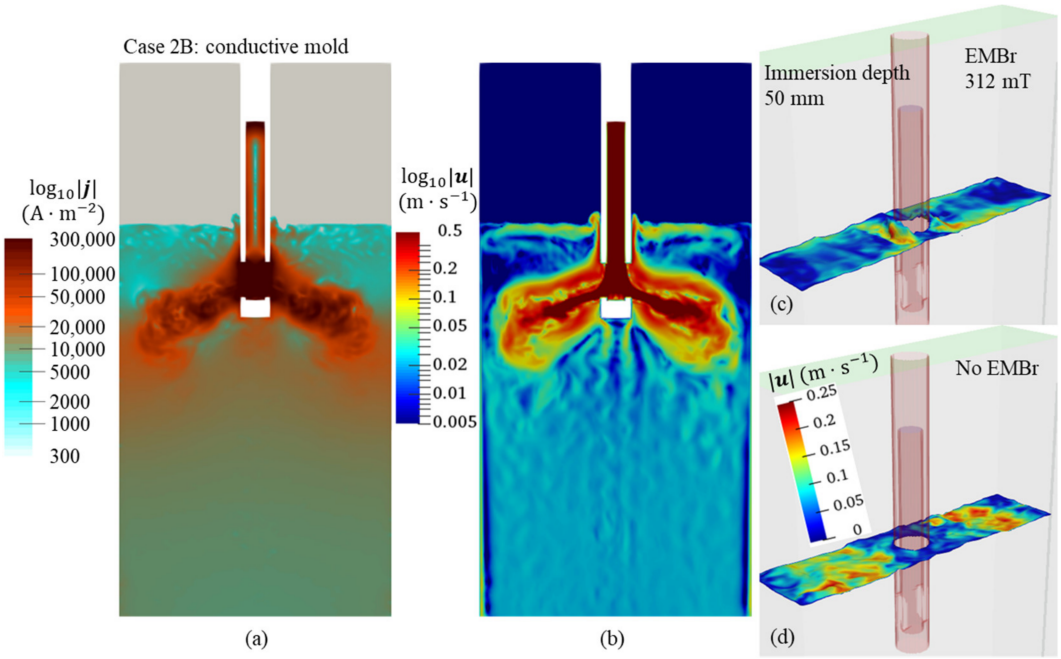


Figure 11. Meniscus flow for Case 2B: (**a**) induced e-current density and (**b**) melt velocity (midplane); (**c**) interface velocity with EMBr compared with (**d**) Case 0B without EMBr.

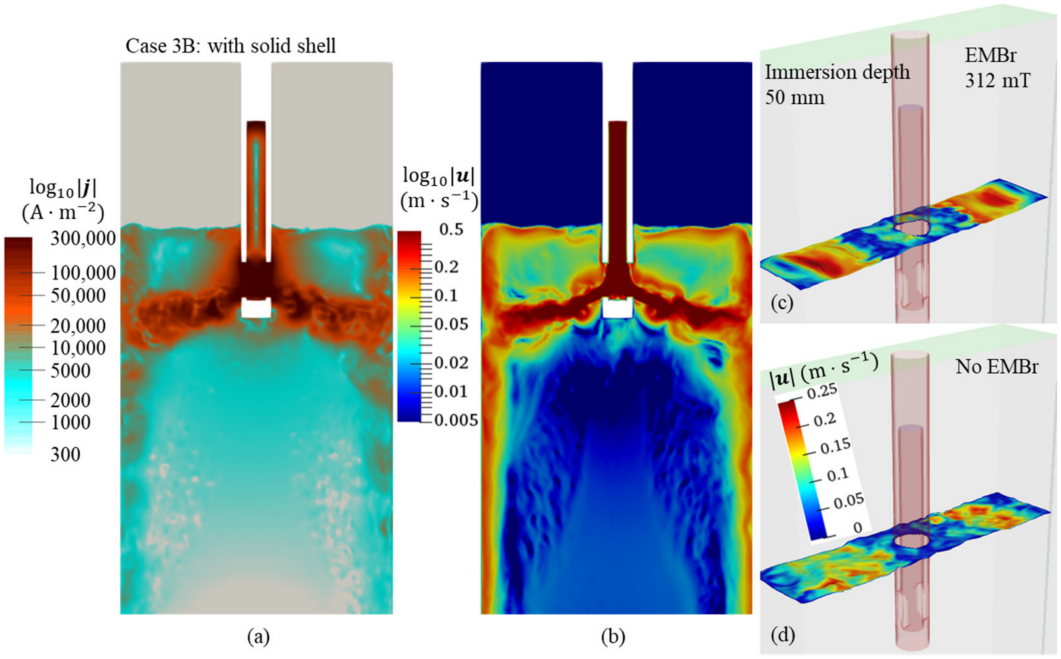


Figure 12. Meniscus flow for Case 3B: (**a**) induced e-current density and (**b**) melt velocity (midplane); (**c**) interface velocity with EMBr compared with (**d**) Case 0B without EMBr.

4. Discussion

Herein, to understand the impact of EMBr on the free surface behavior in the CC mold, the characteristics of the MHD flow, such as turbulent structures, time-averaged streamlines, and the power spectral density, are presented.

4.1. MHD Turbulence

The second invariant of the velocity gradient, known as Q-criterion ($\mathcal{Q}_{\text{crit}}$),

$$\mathcal{Q}_{\text{crit}} = \frac{1}{2}[(\text{tr}\ (\nabla \boldsymbol{u})\ )^2 - \text{tr}\ (\nabla \boldsymbol{u} \bullet \nabla \boldsymbol{u})], \tag{18}$$

is commonly employed to identify flow turbulence [48,49].

The modeling results for the two-phase flow without EMBr and for the cases with the applied magnetic field are shown in Figures 13 and 14. The turbulent structures, bounded by the iso-surface $Q_{\text{crit}} = 100$, with the corresponding instantaneous meniscus velocity and free surface profile, are shown.

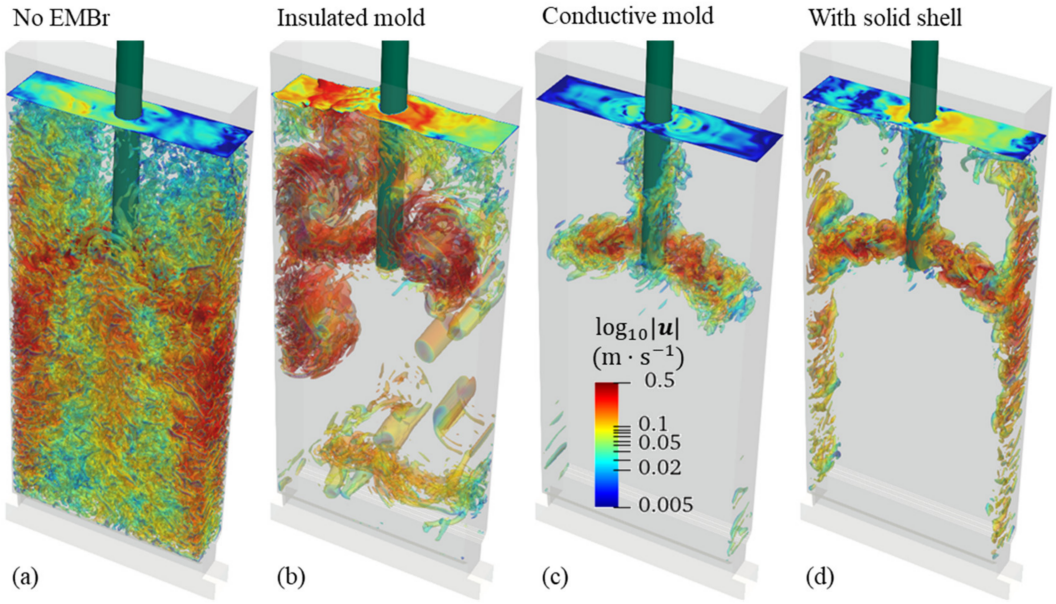


Figure 13. Turbulent flow structures ($Q_{\text{crit}} = 100$), SEN immersion depth of 100 mm: (**a**) Case 0A; (**b**) Case 1A; (**c**) Case 2A; (**d**) Case 3A.

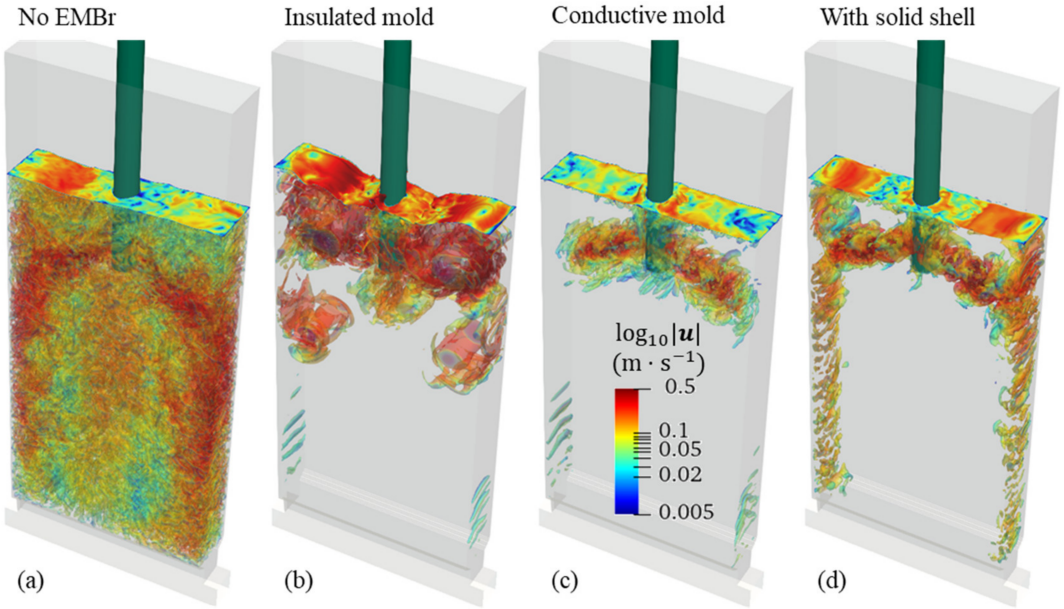


Figure 14. Turbulent flow structures ($Q_{\text{crit}} = 100$), SEN immersion depth of 50 mm (**a**) Case 0B; (**b**) Case 1B; (**c**) Case 2B; (**d**) Case 3B.

Except in Case 1A with the insulated mold (Figure 13b), the top surface remains dominantly flat for the 100 mm immersion depth of the SEN. The non-EMBr turbulence rate (Figure 13a) is significantly dampened under the applied magnetic field. As it was shown by Davidson [35] and Kobayashi [50], tridimensional turbulence rearranges into coherent quasi-2D structures aligned with the magnetic field.

In Case 1A, the insulated mold (Figure 13b) leads to the formation of self-inducing MHD vortices that tightly interact with the meniscus, causing its distortion and waving. It is observed that the highly turbulent flow structure without EMBr is restructured to the combination of the submeniscus coherent rolls dominantly aligned along the applied magnetic field direction.

The formation of the anisotropic 2D turbulence also results in the redistribution of the linear momentum and the unexpected acceleration of the meniscus, as can be found elsewhere [23], and was recently investigated using a single phase approach [26].

In Case B with the shallow SEN immersion depth in Figure 14, the strong interaction of the jet flow with the free surface appears for all cases. Interestingly, the coherent self-inducing MHD vortices in nonconductive Case 1B (Figure 14b) are concentrated and restricted under the meniscus, causing extreme waving that periodically leads to air bubble entrapment (see Figure 10c).

A returbulization of the melt flow occurs near the narrow wall at the domain bottom for Case 2A (Figure 13b,c), Case 1B (Figure 14b), and Case 2B (Figure 14c). That happens due to the weakened EMBr field and the release of the braking action.

4.2. Time-Averaged Flow Field

The stream-lines of the time-averaged velocity field of the melt are shown for the deep immersion depth in Figure 15 and for the shallow one in Figure 16. The stream-lines are shown in the midplane and are colored by velocity magnitude. The flow direction is indicated using black arrows.

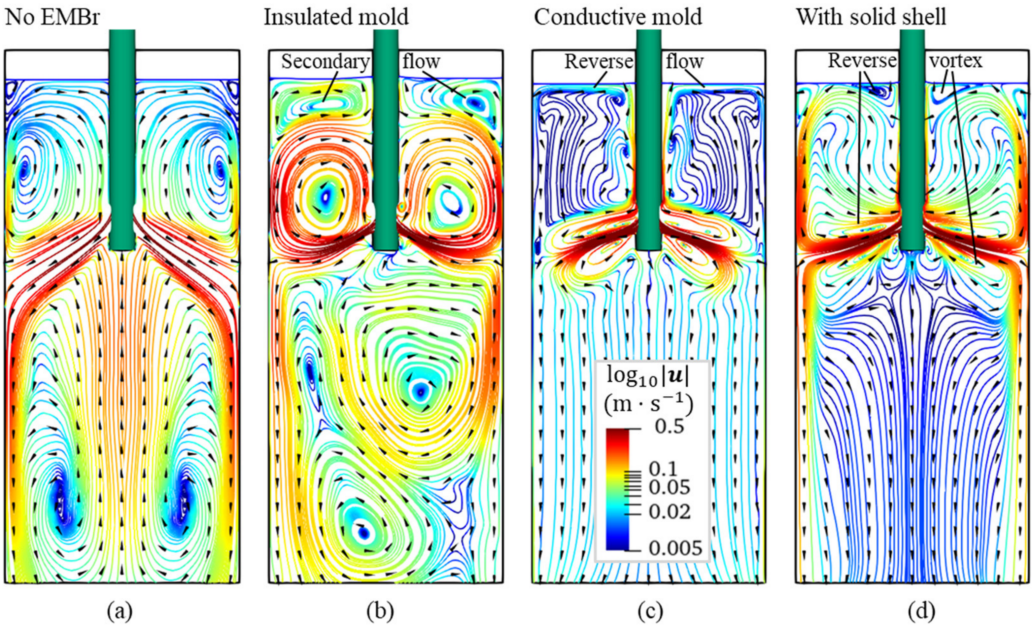


Figure 15. Time averaged velocity stream-lines (midplane), SEN immersion depth of 100 mm: (**a**) Case 0A; (**b**) Case 1A; (**c**) Case 2A; (**d**) Case 3A.

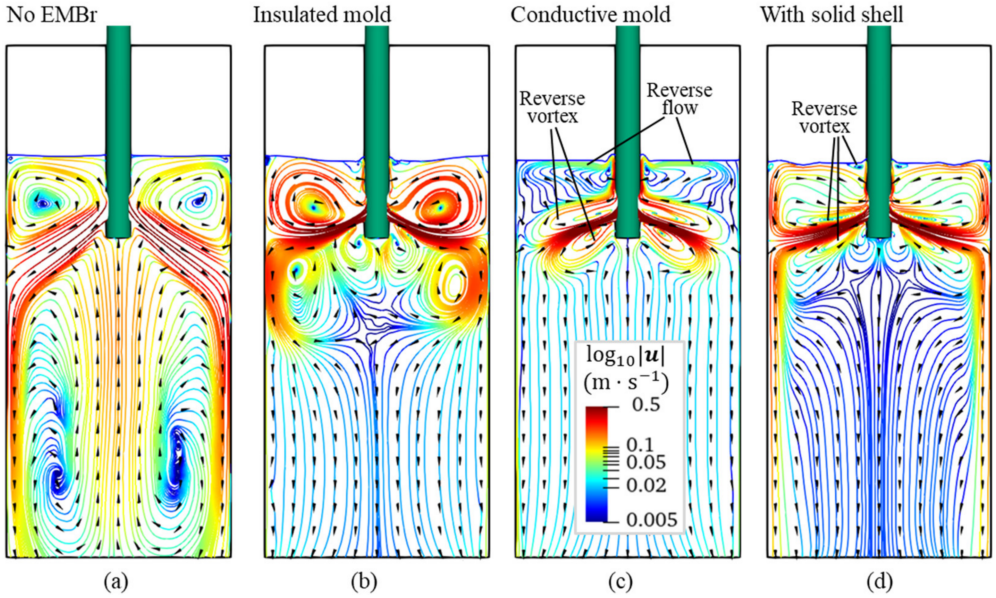


Figure 16. Time averaged velocity stream-lines (midplane), SEN immersion depth of 50 mm: (**a**) Case 0B; (**b**) Case 1B; (**c**) Case 2B; (**d**) Case 3B.

The formation of the reverse flow zones above and below the feeding jets is clearly observed in Figures 15c,d and 16c,d, supported by the flattening of the jets [34] that are referred to as banana-shaped [51]. For the deep immersion depth shown in Figure 15b, two rolls are developed directly under the meniscus surface, opposing the main double-roll flow beneath. Thereby, an alternation of the general flow pattern occurs with varying SEN immersion depth.

In Case 2A (Figure 15c) and Case 2B (Figure 16c), a thin reverse meniscus flow is detected. It is defined by the complex Lorentz force topology, resulting in the formation of reverse vortices above and below jets and upward flow along the insulated SEN.

In Figure 15d (Case 3A), an initial formation of the opposite vortex above the SEN ports toward the meniscus surface is observed. Additionally, mold corner rolls are generated, as previously discussed elsewhere [26]. They are damped for the shallower SEN immersion depth (see Case 3B in Figure 16d) by the wavy free surface.

4.3. Power Spectral Density Analysis

The flow velocity statistics were also collected during the simulation. The flow velocity was monitored at the point P1 in Figure 1a with a sampling frequency of 2×10^4 Hz. That corresponds as known from the signal processing theory to the resolved Fourier spectrum with the maximum frequency of 1×10^4 Hz. The monitoring point P1 corresponds to the jet impact region in the mold. The obtained signal was analyzed and displayed using the open-source statistical computing and graphics language R [52].

The turbulent spectrum results are presented in Figures 17 and 18. They combine the captured time series of the velocity magnitude with the corresponding moving average (MA), displayed in the top subfigures with index 1, as in Figure 17a1 for the non-EMBr case. A time interval $\Delta t = 0.2$ sec was used for the MA calculations. An 8 s interval is presented to detail velocity oscillations. The total of 39 sampled seconds corresponds to a triple characteristic time (see Equation (20) in Vakhrushev et al. [25]).

The power spectral density (PSD) is shown in the bottom subfigures, such as Figure 17a2. The frequency and PSD axes are log-scaled for clarity.

The PSD periodogram has a significant drawback. It does not become smoother as the length of the time series increases. It includes more spikes packed closer together, which complicates the dominant frequency search. The remedy is to smooth the periodogram. In the presented study, a smoothing kernel with a span of 3 spikes was applied in the *spectrum*

package of the R language [52]. The smoothed PSD is used hereafter. The red line marks the dominant frequency f_1 on a PSD periodogram.

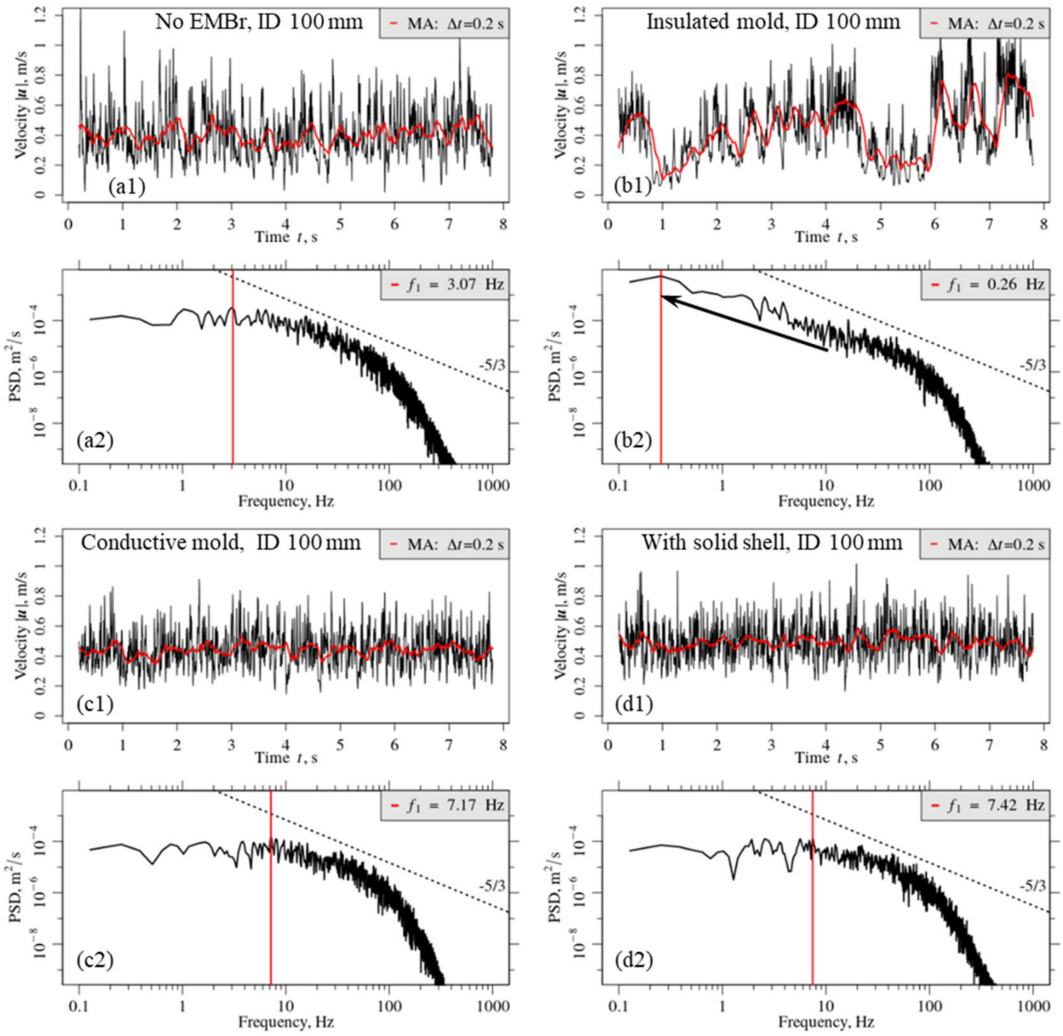


Figure 17. Instantaneous velocity at the monitor point P1 with moving average (top subfigures) and corresponding PSD (bottom subfigures), immersion depth (ID) of 100 mm: (**a1**,**a2**) Case 0A; (**b1**,**b2**) Case 1A; (**c1**,**c2**) Case 2A; (**d1**,**d2**) Case 3A.

The PSD units are $m^2/s \sim |\boldsymbol{u}|^2/f$, where f is a frequency. The PSD is the flow kinetic energy density per frequency unit and represents the distribution of the turbulent flow energy between big, slow structures on the left and fast, small ones on the right. The frequencies are cut to 1×10^3 Hz to focus on a region of interest. The black dash line on the PSD plots associates with the -5/3 logarithmic decay in the inertial range of the Kolmogorov's energy cascade.

The black arrows in the spectral diagrams in Figures 17 and 18 indicate significant changes in the energy spectrum. In Figure 18, presenting cases with the shallow immersion depth, the arrows are used in the comparison to the results for the cases with the SEN position at 100 mm, shown in Figure 17.

To start with non-EMBr Case 0A (immersion depth of 100 mm), a power spectrum of the velocity signal is obtained with the uniform PSD distribution in the energy containing scale for the frequency below 10 Hz (see Figure 17a2). A corresponding $-5/3$ logarithmic decay is detected for the higher frequencies in the inertial range in Figure 17a2.

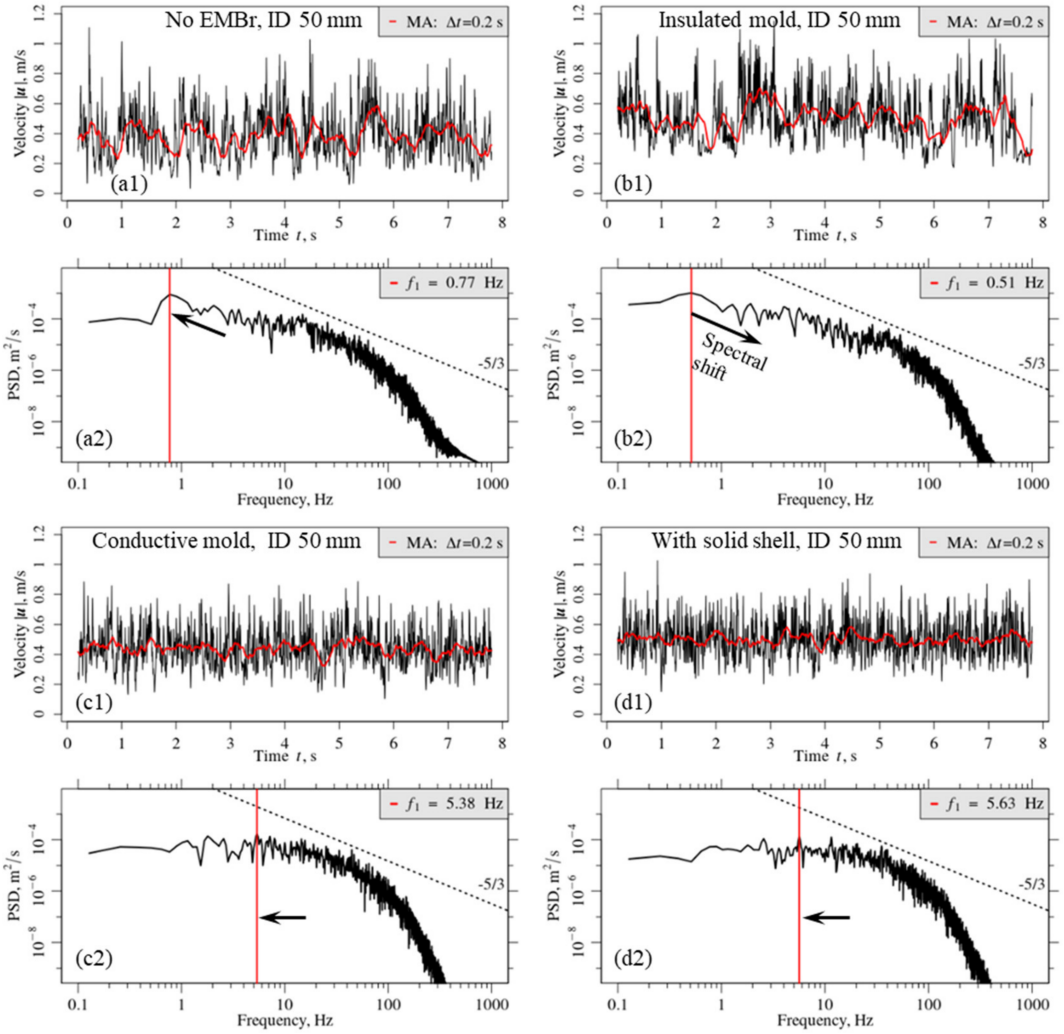


Figure 18. Instantaneous velocity at the monitor point P1 with moving average (top subfigures) and corresponding PSD (bottom subfigures), immersion depth (ID) of 50 mm: (**a1**,**a2**) Case 0B; (**b1**,**b2**) Case 1B; (**c1**,**c2**) Case 2B; (**d1**,**d2**) Case 3B.

The transient velocity oscillations have a higher amplitude and distinctive low frequency fluctuations in Case 1A with the insulated mold (Figure 17b1). The significant difference in the PSD distribution is detected on the periodogram in Figure 17b2. A shift towards big slow structures is marked with a long black arrow. These are the self-inducing MHD coherent structures with a characteristic period of 4 s, shown earlier in Figures 7b, 13b and 15b. The PSD of the dominant frequency (f_1) for the Case 1A in Figure 17b2 is 1–2 orders of magnitude higher than in other scenarios.

When the conductive or semi-conductive molds are considered, the oscillation amplitudes decrease, slow fluctuations are damped, and the dominant frequencies f_1 grow from 3 Hz in Figure 17a2 up to 7 Hz in Figure 17c2,d2.

The velocity time series and the spectral results for the shallow SEN position at 50 mm are gathered in Figure 18. The main flow oscillation frequency f_1 for the non-EMBr scenario (Figure 18a2), for Cases 2B (Figure 18c2), and for Case 3B (Figure 18d2) shifts toward lower values. The free surface wave interacts with the feeding jet fluctuations at probing location P1.

The development of the meniscus waving effect is especially noticeable for the non-EMBr case in Figure 18a2, where the PSD gets a strong kink at the frequencies around 0.77 Hz in comparison to the spectral distribution for the previous results in Figure 17a2.

As shown in Figure 17b2, the bigger and slower MHD vortices ($f_1 = 0.26$ Hz), carry more energy in Case 1A with a deeper immersion depth in comparison to the shallower meniscus in Case 2B (Figure 18b2). The frequency f_1 of the maximum PSD value in Figure 18b2 increases to 0.51 Hz, and the whole energy spectrum redistributes towards higher frequencies. That implies that the formation of the self-inducing vortex structures is restricted by the vicinity of the free surface; see also Figure 14b. The waving leads to the collapsing and destruction of the MHD vortices. As a result, the energy of the slowest vortices decreases, and the energy distribution shifts towards a faster spectral range.

One would slower oscillations in Case 3B with the semi-conductive shell (Figure 18d2) in comparison to Case 2B with the perfectly conductive mold (Figure 18c2) since the braking effect is weakened. However, the flow patterns, shown in Figure 16c,d, are totally different. The opposite (calmer) meniscus flow promoted by the reverse flow zones along the jets [26,34] in Figure 16c interacts with the feeding jets. For Case 3B in Figure 16d, the standard double roll pattern occurs, which is affected by the stronger meniscus waving due to the finite conductance ratio of the attached solid shell. Thus, a direct comparison of the PSD is not possible.

5. Conclusions

The free surface modelling, based on the mini-LIMMCAST experiment in the Helmholtz-Zentrum Dresden-Rossendorf, was performed using VOF method and LES approach to simulate a turbulent MHD flow. The numerical model was verified against the experimental measurements and single-phase simulations.

This study newly combines a single mesh approach, introduced previously in Vakhrushev et al. [25], with the VOF interface tracking to include the presence of a conductive shell. The harmonic interpolation of the electrical conductivity was applied to precisely calculate the induced e-currents at the conductive/dielectric phase interface.

The consistent simulation series of the turbulent flow with and without the EMBr were included in a comparative study. Cases with an immersion depth, which is more realistic for the CC process, were added to the SEN positioning from the experiment.

The study includes scenarios for the electrically insulating, perfectly conductive, and semi-conductive domain boundaries. The multiphase MHD flow parameters, such as velocity, liquid fraction, and induced e-current density, are presented and analyzed together with the turbulent characteristics and power spectral density for all listed cases.

We found that for the deep SEN immersion depth of 100 mm, the MHD forces do not play a considerable role for the conductive and semi-conductive mold. Initially stable meniscus remains calm. For the insulated mold case, the self-inducing coherent MHD structures, aligned with the applied magnetic field, strongly distort the meniscus.

More pronounced MHD effects are detected at the immersion depth of 50 mm. The action of the Lorentz force in the nonconductive mold causes strong waving of the meniscus and leads to the entrapment of air bubbles in the submeniscus melt flow. In the case of the conductive mold, an opposing meniscus flow develops, which interacts with the feeding jets. When the semi-conductive solid shell is attached to the mold walls, a classical double-roll pattern is observed. The upward vortex, generated by the reverse flow zone above and below the feeding jets, can initiate the opposite flow in the upper region of the CC mold. The secondary MHD structures, opposing the main double-roll pattern, are formed under specific conditions for the deeper SEN immersion depth.

The PSD is strongly shifted toward the slower structures in the case of the insulated mold. However, for the shallow immersion depth, the MHD vortices are destructed in the meniscus vicinity, and the PSD redistributes to the faster frequency range.

As shown, the free surface modelling results fully depend on the SEN immersion depth and assumed electrical conductivity of the mold. A common practice to neglect the presence of the semi-conductive shell by simplifying the problem to a perfectly insulated or conductive mold does not reflect a physical phenomenon in the real casting.

The authors highly encourage the readers to check the Supplementary Videos, which highlight the dynamics of the MHD flow including free surface behavior.

Supplementary Materials: The following supporting information can be downloaded at: https://www.mdpi.com/article/10.3390/met13030444/s1, Video S1: MHD flow with electrically insulated mold and immersion depth of 100 mm. Video S2: MHD flow with electrically insulated mold and immersion depth of 50 mm. Video S3: MHD flow at presence of semi-conductive shell and immersion depth of 100 mm. Video S4: MHD flow at presence of semi-conductive shell and immersion depth of 50 mm.

Author Contributions: Conceptualization, methodology, software, writing—original draft preparation, A.V., E.K.-S. and J.B.; writing—review and editing, A.K., M.W. and A.L.; reviewing and analysis, Y.T., G.H., G.N. and J.W. All authors have read and agreed to the published version of the manuscript.

Funding: This research received no external funding.

Institutional Review Board Statement: Not applicable.

Informed Consent Statement: Not applicable.

Data Availability Statement: Not applicable.

Acknowledgments: The authors acknowledge the financial support by the Austrian Federal Ministry of Economy, Family and Youth and the National Foundation for Research, Technology and Development within the framework of the Christian Doppler Laboratory for Metallurgical Applications of Magnetohydrodynamics. This work was supported by the Ministry of Education, Youth and Sports of the Czech Republic under the grant number 8J22AT009 as well as by the Federal Ministry of Education, Science and Research (BMBWF) of Austria under the grant number WTZ OEAD CZ10/2022.

Conflicts of Interest: The authors declare no conflict of interest.

References

1. Lee, P.D.; Ramirez-Lopez, P.E.; Mills, K.C.; Santillana, B. Review: The "Butterfly Effect" in Continuous Casting. *Ironmak. Steelmak.* **2012**, *39*, 244–253. [CrossRef]
2. Mills, K.C.; Ramirez-Lopez, P.; Lee, P.D.; Santillana, B.; Thomas, B.G.; Morales, R. Looking into Continuous Casting Mould. *Ironmak. Steelmak.* **2014**, *41*, 242–249. [CrossRef]
3. Lopez, P.E.R.; Jalali, P.N.; Björkvall, J.; Sjöström, U.; Nilsson, C. Recent Developments of a Numerical Model for Continuous Casting of Steel: Model Theory, Setup and Comparison to Physical Modelling with Liquid Metal. *ISIJ Int.* **2014**, *54*, 342–350. [CrossRef]
4. Thomas, B.G. Review on Modeling and Simulation of Continuous Casting. *Steel Res. Int.* **2018**, *89*, 1700312. [CrossRef]
5. Hibbeler, L.C.; Thomas, B.G. Mold Slag Entrainment Mechanisms in Continuous Casting Molds. *Iron Steel Technol.* **2013**, *10*, 121–136.
6. Liu, Z.; Li, B.; Vakhrushev, A.; Wu, M.; Ludwig, A. Physical and Numerical Modeling of Exposed Slag Eye in Continuous Casting Mold Using Euler–Euler Approach. *Steel Res. Int.* **2019**, *90*, 1800117. [CrossRef]
7. Srivastava, A.; Chattopadhyay, K. Macroscopic Mechanistic Modeling for the Prediction of Mold Slag Exposure in a Continuous Casting Mold. *Met. Mater. Trans. B* **2022**, *53*, 1018–1035. [CrossRef]
8. Iguchi, M.; Yoshida, J.; Shimizu, T.; Mizuno, Y. Model Study on the Entrapment of Mold Powder into Molten Steel. *ISIJ Int.* **2000**, *40*, 685–691. [CrossRef]
9. Yamashita, S.; Iguchi, M. Mechanism of Mold Powder Entrapment Caused by Large Argon Bubble in Continuous Casting Mold. *ISIJ Int.* **2001**, *41*, 1529–1531. [CrossRef]
10. Yoshida, J.; Ohmi, T.; Iguchi, M. Cold Model Study of the Effects of Density Difference and Blockage Factor on Mold Powder Entrainment. *ISIJ Int.* **2005**, *45*, 1160–1164. [CrossRef]
11. Kasai, N.; Iguchi, M. Water-Model Experiment on Melting Powder Trapping by Vortex in the Continuous Casting Mold. *ISIJ Int.* **2007**, *47*, 982–987. [CrossRef]
12. Hagemann, R.; Schwarze, R.; Heller, H.P.; Scheller, P.R. Model Investigations on the Stability of the Steel-Slag Interface in Continuous-Casting Process. *Met. Mater. Trans. B* **2013**, *44*, 80–90. [CrossRef]
13. Saeedipour, M.; Puttinger, S.; Doppelhammer, N.; Pirker, S. Investigation on Turbulence in the Vicinity of Liquid-Liquid Interfaces—Large Eddy Simulation and PIV Experiment. *Chem. Eng. Sci.* **2019**, *198*, 98–107. [CrossRef]
14. Puttinger, S.; Saeedipour, M. Time-Resolved PIV Measurements of a Deflected Submerged Jet Interacting with Liquid-Gas and Liquid-Liquid Interfaces. *Exp. Comput. Multiph. Flow* **2022**, *4*, 175–189. [CrossRef]
15. Bernhard, C.; Hiebler, H.; Wolf, M.M. How Fast Can We Cast? *Ironmak. Steelmak.* **2000**, *27*, 450–454. [CrossRef]

16. SenGupta, A.; Santillana, B.; Sridhar, S.; Auinger, M. A Multiscale-Based Approach to Understand Dendrite Deflection in Continuously Cast Steel Slab Samples. *Met. Mater. Trans. A* **2021**, *52*, 3413–3422. [CrossRef]
17. Wang, C.; Liu, Z.; Li, B. Combined Effects of EMBr and SEMS on Melt Flow and Solidification in a Thin Slab Continuous Caster. *Metals* **2021**, *11*, 948. [CrossRef]
18. Vakhrushev, A.; Kharicha, A.; Karimi-Sibaki, E.; Wu, M.; Ludwig, A.; Nitzl, G.; Tang, Y.; Hackl, G.; Watzinger, J. Modeling Asymmetric Flow in the Thin-Slab Casting Mold under Electromagnetic Brake. *Steel Res. Int.* **2022**, *93*, 2200088. [CrossRef]
19. Lu, H.; Zhong, Y.; Ren, W.; Ren, Z.; Lei, Z. Effect of Electromagnetic Brake on Transient Asymmetric Flow, Solidification, and Inclusion Transport in a Slab Continuous Casting. *Steel Res. Int.* **2022**, *93*, 2200518. [CrossRef]
20. Timmel, K.; Eckert, S.; Gerbeth, G. Experimental Investigation of the Flow in a Continuous-Casting Mold under the Influence of a Transverse, Direct Current Magnetic Field. *Met. Mater. Trans. B* **2011**, *42*, 68–80. [CrossRef]
21. Timmel, K.; Kratzsch, C.; Asad, A.; Schurmann, D.; Schwarze, R.; Eckert, S. Experimental and Numerical Modeling of Fluid Flow Processes in Continuous Casting: Results from the LIMMCAST-Project. *IOP Conf. Ser. Mater. Sci. Eng.* **2017**, *228*, 012019. [CrossRef]
22. Chaudhary, R.; Ji, C.; Thomas, B.G.; Vanka, S.P. Transient Turbulent Flow in a Liquid-Metal Model of Continuous Casting, Including Comparison of Six Different Methods. *Met. Mater. Trans. B* **2011**, *42*, 987–1007. [CrossRef]
23. Thomas, B.G.; Singh, R.; Vanka, S.P.; Timmel, K.; Eckert, S.; Gerbeth, G. Effect of Single-Ruler Electromagnetic Braking (EMBr) Location on Transient Flow in Continuous Casting. *J. Manuf. Sci. Prod.* **2015**, *15*, 93–104. [CrossRef]
24. Liu, Z.; Vakhrushev, A.; Wu, M.; Karimi-Sibaki, E.; Kharicha, A.; Ludwig, A.; Li, B. Effect of an Electrically-Conducting Wall on Transient Magnetohydrodynamic Flow in a Continuous-Casting Mold with an Electromagnetic Brake. *Metals* **2018**, *8*, 609. [CrossRef]
25. Vakhrushev, A.; Kharicha, A.; Liu, Z.; Wu, M.; Ludwig, A.; Nitzl, G.; Tang, Y.; Hackl, G.; Watzinger, J. Electric Current Distribution During Electromagnetic Braking in Continuous Casting. *Met. Mater. Trans. B* **2020**, *51*, 2811–2828. [CrossRef]
26. Vakhrushev, A.; Kharicha, A.; Karimi-Sibaki, E.; Wu, M.; Ludwig, A.; Nitzl, G.; Tang, Y.; Hackl, G.; Watzinger, J.; Eckert, S. Generation of Reverse Meniscus Flow by Applying an Electromagnetic Brake. *Met. Mater. Trans. B* **2021**, *52*, 3193–3207. [CrossRef]
27. Asad, A.; Kratzsch, C.; Schwarze, R. Numerical Investigation of the Free Surface in a Model Mold. *Steel Res. Int.* **2016**, *87*, 181–190. [CrossRef]
28. Weller, H.G.; Tabor, G.; Jasak, H.; Fureby, C. A Tensorial Approach to Computational Continuum Mechanics Using Object-Oriented Techniques. *Comput. Phys.* **1998**, *12*, 620. [CrossRef]
29. Saeedipour, M.; Vincent, S.; Pirker, S. Large Eddy Simulation of Turbulent Interfacial Flows Using Approximate Deconvolution Model. *Int. J. Multiph. Flow* **2019**, *112*, 286–299. [CrossRef]
30. Roenby, J.; Bredmose, H.; Jasak, H. A Computational Method for Sharp Interface Advection. *R. Soc. Open Sci.* **2016**, *3*, 160405. [CrossRef]
31. Gamet, L.; Scala, M.; Roenby, J.; Scheufler, H.; Pierson, J.-L. Validation of Volume-of-Fluid OpenFOAM® IsoAdvector Solvers Using Single Bubble Benchmarks. *Comput. Fluids* **2020**, *213*, 104722. [CrossRef]
32. Esteban, A.; López, J.; Gómez, P.; Zanzi, C.; Roenby, J.; Hernández, J. A Comparative Study of Two Open-Source State-of-the-Art Geometric VOF Methods. *Comput. Fluids* **2023**, *250*, 105725. [CrossRef]
33. Smolyanov, I.A.; Shmakov, E.I.; Baake, E.; Guglielmi, M. Verification of the Code to Calculate Duct Flow Affected by External Magnetic Field. *Comp. Contin. Mech.* **2021**, *14*, 322–332. [CrossRef]
34. Kharicha, A.; Vakhrushev, A.; Karimi-Sibaki, E.; Wu, M.; Ludwig, A. Reverse Flows and Flattening of a Submerged Jet under the Action of a Transverse Magnetic Field. *Phys. Rev. Fluids* **2021**, *6*, 123701. [CrossRef]
35. Davidson, P.A. *An Introduction to Magnetohydrodynamics*, 1st ed.; Cambridge University Press: Cambridge, UK, 2001; ISBN 978-0-521-79487-9.
36. Ni, M.-J.; Munipalli, R.; Huang, P.; Morley, N.B.; Abdou, M.A. A Current Density Conservative Scheme for Incompressible MHD Flows at a Low Magnetic Reynolds Number. Part II: On an Arbitrary Collocated Mesh. *J. Comput. Phys.* **2007**, *227*, 205–228. [CrossRef]
37. Hirt, C.W.; Nichols, B.D. Volume of Fluid (VOF) Method for the Dynamics of Free Boundaries. *J. Comput. Phys.* **1981**, *39*, 201–225. [CrossRef]
38. Ubbink, O. Numerical Prediction of Two Fluid Systems with Sharp Interfaces. Ph.D. Thesis, Imperial College of Science, London, UK, 1997.
39. Ubbink, O.; Issa, R.I. A Method for Capturing Sharp Fluid Interfaces on Arbitrary Meshes. *J. Comput. Phys.* **1999**, *153*, 26–50. [CrossRef]
40. Vakhrushev, A.; Menghuai, W.; Ludwig, A.; Tang, Y.; Nitzl, G.; Hackl, G. Experimental Verification of the 3-Phase Continuous Casting Simulation Using a Water Model. In Proceedings of the 8th ECCC Conference, on Storage Device, Graz, Austria, 23–26 June 2014; p. 10.
41. Brackbill, J.U.; Kothe, D.B.; Zemach, C. A Continuum Method for Modeling Surface Tension. *J. Comput. Phys.* **1992**, *100*, 335–354. [CrossRef]
42. Boris, J.P.; Book, D.L. Flux-Corrected Transport. I. SHASTA, a Fluid Transport Algorithm That Works. *J. Comput. Phys.* **1973**, *11*, 38–69. [CrossRef]

43. Zalesak, S.T. Fully Multidimensional Flux-Corrected Transport Algorithms for Fluids. *J. Comput. Phys.* **1979**, *31*, 335–362. [CrossRef]
44. Vakhrushev, A.; Kharicha, A.; Liu, Z.; Wu, M.; Ludwig, A.; Nitzl, G.; Tang, Y.; Hackl, G.; Watzinger, J. Optimizing the Flow Conditions in the Thin-Slab Casting Mold Using Electromagnetic Brake. In Proceedings of the 8th International SteelSim Conference, AIST, Toronto, ON, Canada, 13–15 August 2019; pp. 615–619.
45. Vakhrushev, A.; Kharicha, A.; Wu, M.; Ludwig, A.; Nitzl, G.; Tang, Y.; Hackl, G.; Watzinger, J.; Rodrigues, C.M.G. Modelling Viscoplastic Behavior of Solidifying Shell under Applied Electromagnetic Breaking during Continuous Casting. *IOP Conf. Ser. Mater. Sci. Eng.* **2020**, *861*, 012015. [CrossRef]
46. Plevachuk, Y.; Sklyarchuk, V.; Eckert, S.; Gerbeth, G.; Novakovic, R. Thermophysical Properties of the Liquid Ga–In–Sn Eutectic Alloy. *J. Chem. Eng. Data* **2014**, *59*, 757–763. [CrossRef]
47. Pawar, S.D.; Murugavel, P.; Lal, D.M. Effect of Relative Humidity and Sea Level Pressure on Electrical Conductivity of Air over Indian Ocean. *J. Geophys. Res.* **2009**, *114*, D02205. [CrossRef]
48. Hunt, J.C.R.; Wray, A.A.; Moin, P. Eddies, Streams, and Convergence Zones in Turbulent Flows. In Proceedings of the Summer Program 1988, Center for Turbulence Research Report CTR-S88, Stanford, CA, USA, 27 June–22 July 1988; pp. 193–208.
49. Kolář, V. Vortex Identification: New Requirements and Limitations. *Int. J. Heat Fluid Flow* **2007**, *28*, 638–652. [CrossRef]
50. Kobayashi, H. Large Eddy Simulation of Magnetohydrodynamic Turbulent Channel Flows with Local Subgrid-Scale Model Based on Coherent Structures. *Phys. Fluids* **2006**, *18*, 045107. [CrossRef]
51. Schurmann, D.; Glavinić, I.; Willers, B.; Timmel, K.; Eckert, S. Impact of the Electromagnetic Brake Position on the Flow Structure in a Slab Continuous Casting Mold: An Experimental Parameter Study. *Met. Mater. Trans. B* **2020**, *51*, 61–78. [CrossRef]
52. R Core Team. *R: A Language and Environment for Statistical Computing*; R Foundation for Statistical Computing: Vienna, Austria, 2022.

Disclaimer/Publisher's Note: The statements, opinions and data contained in all publications are solely those of the individual author(s) and contributor(s) and not of MDPI and/or the editor(s). MDPI and/or the editor(s) disclaim responsibility for any injury to people or property resulting from any ideas, methods, instructions or products referred to in the content.